



# Performance evaluation of an integrated path differential absorption LIDAR model for surface pressure from low-Earth orbit

Guanglie Hong<sup>1</sup>, Yu Dong<sup>2</sup>, Huige Di<sup>2</sup>

<sup>1</sup>Shanghai Institute of Technical Physics, Chinese Academy of Sciences, Shanghai, 200083, China

<sup>2</sup>Xi'an University of Technology, Xi'an, 710048, China

Correspondence to: Dong Yu (dy\_raister@163.com), Di Huige (dihuige@xaut.edu.cn)

**Abstract.** Remote sensing of surface pressure from space is critical; differential absorption LIDAR and differential absorption radar are only two kinds of remote sensing instruments with this potential. The differential absorption LIDAR works in integral path mode from the satellite in low-Earth orbit. It measures the differential optical depth of the Oxygen A-band, and the surface pressure is thereafter obtained by performing circle-iterative calculation. Performance evaluation of the differential absorption LIDAR model was conducted with respect to the advanced system parameters of the space instrument, Low echo pulse energy at ocean surface and the challenging calculation of repetitive cumulative average of echo on uneven land surface yielded random errors in surface pressure measurement. On the other hand, uncertain atmospheric temperature and water vapor mixture profiles resulted in systematic error of surface pressure. Consequently, controlling the error of surface pressure within 0.1% proved challenging. Under a strict implementation of the error budget, the time resolution is 6.25 s and along-orbit distance resolution is 44km, and the results showed that 765.6735/765.4637 nm is suitable as the working wavelength pair. Further, error could be expected to within 0.2–0.3% for the cumulative average of 625 ocean surface laser pulse echoes, cumulative average of more than 144 pulse echoes on land, and observation from the 400km orbit.

## 1 Introduction

Atmospheric pressure plays a vital role in several atmospheric processes related to atmospheric dynamics. Low/high pressure, low pressure troughs, high pressure ridges, and anticyclones and other related information have been introduced into the atmospheric model. Hurricanes are profound low-pressure systems that originate from low-pressure cyclones in the tropical or subtropical oceanic regions. Accurate prediction of their formation, landing direction, and movement trajectory requires atmospheric pressure gradient distribution data. Fundamentally, the density of the atmosphere in high latitudes increase during winter, causing the air to shrink and sink, thereby increasing the pressure and gradually resulting in the formation of a powerful, deep, and broad air mass. Upon the accumulation of a sufficient cold high-pressure force, a cold wave is formed, which rolls out and pours down. Meanwhile, airspace for the release of radio sounding balloons is restricted; thus, continuous detection during the entire day is not possible. Brown et al.(1986) reported that the accuracy of the weather models is primarily limited by the regional sparsity of the input data. Specifically, atmospheric pressure data is very sparse in large areas of the ocean, desert, plateaus, and polar regions. Consequently, the International Meteorological Organization aims to achieve remote sensing of surface pressure at an accuracy of 0.1–0.3%(Korb et al., 1995)(WMO-ICSU, 1973), which however, remains a big challenge.



In 1983, Korb, C. L. et al., (1983) of Laboratory for Atmospheres, NASA Goddard Space Flight Center, proposed a method of detecting atmospheric pressure using differential absorption LIDAR and the trough between oxygen absorption lines. In 1987, Schwemmer et al. (1987) structured a novel differential absorption LIDAR system. It employs a flash-pump alexandrite laser to emit a beam of two wavelengths of approximately  $13160\text{cm}^{-1}$ , coupled with an oxygen photoacoustic absorption cell and a high-precision wavelength meter to stabilize the emission wavelength. Moreover, the seed source is a continuous wave from either a Ti:sapphire single longitudinal mode laser or a diode laser (Schwemmer et al., 1987). In June and July 1989, a series of flight measurement tests were conducted on the east coast of the United States (Korb et al., 1989). In 1999, Flamant, C. N., Schwemmer, G. K., Korb, C. L., Evans, K. D. and Palm, S. P. published their report "Pressure measurements Using and Airborne Differential absorption LIDAR. Part I: Analysis of the systematic error sources," (Flamant et al., 1999) where in the instrumental and systematic error sources of differential absorption LIDAR was analyzed when measuring atmospheric pressure profile.

In the ASCENDS (Active Sensing of  $\text{CO}_2$  Emission over Nights, Days, and Seasons) program, the surface pressure was determined to accurately measure the  $\text{CO}_2$  dry mixing ratio (Zaccheo et al., 2014; Crowell, et al., 2015). Between 2007 and 2013 Stephen, M. Krainak, M. Riris, H. and others of NASA Goddard Space Flight Center and Allan, G. R. of Sigma Space Corporation reported on the use of an aircraft as a platform and transmitter to continuously send out pulse trains of multiple wavelengths of approximately  $764.7\text{nm}$  with the receiver receiving the return echoes. (Stephen et al., 2007-2008; Riris et al., 2012-2013, 2017) Thus, multiple pulse train return signals were accumulated, using which the oxygen absorption spectrum curve of the  $764.5\text{--}764.9\text{nm}$  trough segment was plotted. Subsequently, the differential optical depth of oxygen was calculated from the transmittance curve.

Dual-wavelength (detection/reference wavelengths) laser pulses are launched downwards from the space platform (Millán et al., 2014); consequently, the reflected laser pulses energy from the earth's surface or the top of a cloud are received. Subsequently, the atmospheric optical depth and flight time of the laser pulses passing through the air column are measured. Thus, the atmospheric pressure and altitude of the surface/cloud top can be simultaneously obtained, and the top of the cloud ground can be distinguished from the ground. Such data is meaningful for various meteorological applications. By obtaining the pressure values on the surface and cloud tops and combining the results with a vertical temperature profile obtained from other sensors or weather models and utilizing statistical equations, the vertical profile of atmospheric pressure can be obtained. The differential absorption LIDAR is installed on a sun-synchronous orbit, and it makes a polar orbit around the earth from south to north. It allows much denser surface/cloud top atmospheric pressure data than ground meteorological stations to be obtained.

This paper is structured as follow. Section 1 presents the Introduction, and Section 2, the mechanism of differential absorption LIDAR for detecting surface pressure was introduced. whereas Section 3 evaluates the performance of a differential absorption LIDAR model, Finally, Section 4 presents the summary.

## 2 Mechanism of Differential Absorption LIDAR to Detect Atmospheric Pressure

Differential absorption LIDAR selects two wavelengths in the A absorption band of oxygen ( $759\text{--}770\text{nm}$ ). The laser beam with one wavelength value passes through the atmosphere twice; its absorption coefficient, although insensitive to changes in atmospheric temperature, is sensitive to variations in atmospheric pressure. This wavelength is referred to as the detection wavelength (online). Further, the absorption coefficient of another wavelength from the laser beam passing through the atmosphere twice is relatively smaller, and it is referred to as the reference wavelength (offline), with its value being close to the detection wavelength.



Let the atmospheric pressure at altitude  $R_0$ , where the LIDAR is located, be  $p(R_0)$ ; the atmospheric pressure at altitude  $R$  be  $p(R)$ ; and  $g(z)$  be the gravitational acceleration at altitude  $z$ . The difference in the atmospheric pressure between altitude  $R_0$  and  $R$  is equal to the weight of the air column between  $R_0$  and  $R$  per unit area, where the dry air molecular mass  $m_{dry}=28.9644$  g/mol and water vapor molecular mass  $m_{wv}=18$  g/mol.

Atmospheric quasi-static equation:

$$dp = -n_{dry}(z) \cdot (m_{dry} + m_{wv}\chi_{wv}(z)) \cdot g(z)dz \quad (1)$$

Gas state equation:

$$p(z) = n_{dry}(z) \cdot (1 + \chi_{wv}(z)) \cdot kT(z) \quad (2)$$

$$p(R) = p_{surface} \cdot \exp^{-\int_{R_0}^R \frac{(m_{dry} + m_{wv}\chi_{wv}(z))g(z)}{kT(z)(1 + \chi_{wv}(z))} dz} \quad (3)$$

This integration is performed at an altitude  $z$ ,  $n_{dry}(z)$  is the density of dry air molecules,  $\chi_{wv}(z)$  is the water vapor volume mixing ratio,  $p_{surface}$  is the surface pressure, and  $k$  is the Boltzmann constant. Thus, by remote sensing the weight or mass per unit area of a vertical air column between two altitudes, the difference in atmospheric pressure between these two altitudes can be obtained.

Oxygen is among the most stable components in the atmosphere in terms of space and time.  $n_{O_2}(z)$  is the number density of oxygen molecules at altitude  $z$ . The number of oxygen molecules accounts for a fixed proportion of 20.948% of the number of dry air atmospheric molecules. Further, the optical depth of the atmosphere between  $R_0$  and  $R$  is the integral of its extinction coefficient with respect to the beam path, which can be expressed as

$$OD(R_0, R) = \int_{R_0}^R [\alpha_a(v, z) + \alpha_m(v, z) + n_{O_2}(z)\sigma(v, p(z), T(z))] dz \quad (4)$$

where  $OD$  is the optical depth in Beer's theorem,  $\sigma$  is the absorption cross-section of the oxygen molecule to the A-band  $\lambda$  wavelength, and  $\Delta\sigma$  is the difference  $\sigma(\lambda_{on}, p(z), T(z)) - \sigma(\lambda_{off}, p(z), T(z))$ . Further,  $\alpha_a(\lambda, z)$  and  $\alpha_m(\lambda, z)$  are the aerosol extinction coefficient and the extinction coefficient of atmospheric molecules except for oxygen absorption, respectively, and  $n_{O_2}(z)\sigma(\lambda, p(z), T(z))$  is the oxygen absorption coefficient of the corresponding wavelength. The difference in the single-pass optical depth compared to the dual-wavelength between  $R_0$  and  $R$  is referred to as the differential optical depth  $dOD(R_0, R)$ . Although the weight of the atmospheric column between  $R_0$  and  $R$  per unit area is unknown, the differential optical depth can be expressed as

$$dOD(R_0, R) = \int_{R_0}^R n_{O_2}(z)(\sigma(v_{on}, z) - \sigma(v_{off}, z)) dz \quad (5)$$

$$n_{O_2}(z) = \frac{0.20948p(z)}{kT(z) \cdot (1 + \chi(z))} \quad (6)$$

where  $N_{s,on}(R)/N_{s,off}(R)$  represents the online/offline dual-wavelength echo pulse energy (number of photons) received by the LIDAR, which is expressed using the LIDAR equations as follows:

$$N_{s,on}(R) = \frac{c}{2} \frac{A_r}{R^2} \frac{\rho}{\pi} E_{on} \eta_r \eta_d \times \exp[-2OD(R_0, R)] \quad (7)$$

$$N_{s,off}(R) = \frac{c}{2} \frac{A_r}{R^2} \frac{\rho}{\pi} E_{off} \eta_r \eta_d \times \exp[-2OD(R_0, R)] \quad (8)$$

Where  $E_{on}/E_{off}$  is the energy of a single shot emitted laser for both online/offline. Further,  $\eta_r$  is the receiving efficiency of light beam,  $\eta_d$  is the quantum efficiency of the detector, and  $A_r$  is the effective receiving area of the telescope. In the space-to-earth observation, IPDA, receives return echo from hard targets on the ground, and  $\rho$  represents the reflectivity of ground targets.



The beam of dual-wavelength has the same path, receiving/sending time, footprint, and random process in the atmosphere. Further, except for  $\sigma(\lambda, p(z), T(z))$ , all other parameters are considered to be similar (but not equal). Dividing Eq. (7) by Eq. (8), the differential optical depth can be calculated by measuring the energy of the pulse emitted and the energy of received return echo by the LIDAR as follows:

$$dOD(R_0, R) = -\frac{1}{2} \ln \left\{ \left[ \frac{N_{on}(R)}{N_{off}(R)} \right] \left( \frac{E_{off}}{E_{on}} \right) \right\} + C \quad (9)$$

$$C = \int_{R_0}^R [\alpha_a(v_{on}, z) - \alpha_a(v_{off}, z)] dz + \int_{R_0}^R [\alpha_m(v_{on}, z) - \alpha_m(v_{off}, z)] dz \quad (10)$$

where  $C$  represents a systematic error between the  $\frac{1}{2} \ln \left( \frac{N_{off}(R)}{N_{on}(R)} \frac{E_{on}}{E_{off}} \right)$  value calculated from the LIDAR data and the differential optical depth. Thus, laser shots of these two wavelengths are simultaneously emitted and the reflections from the surface/cloud tops are received. However, owing to the difference in oxygen absorption, the atmospheric transmittance of the two wavelengths is different. The logarithm of the ratio of  $\frac{N_{off}(R)}{N_{on}(R)} \frac{E_{on}}{E_{off}}$  can be used to obtain the atmospheric differential optical depth from the satellite to the surface/cloud top. IPDA launches several laser pulses from the space platform to the ground, and it detects the surface pressure, with point  $R_0$  representing the satellite location. Further, there is almost no air pressure  $p(R_0)=0.0$ , and  $p(R)$  represents the surface pressure  $p_{surface}$ .

In the path of the laser beam, only the section from the altitude of 71km to the ground has a significant effect on the optical depth, whereas the effect of atmosphere above 71km can be ignored. Further, the gravitational acceleration  $g(z)$  can be regarded as a constant 9.80616 N/m<sup>2</sup> at atmospheric altitude below 71 km.

On transforming the elevation  $z$  coordinates in Eq. (1) into atmospheric pressure  $p$  coordinates, the following is obtained

$$n_{dry}(z)dz = \frac{dp}{(m_{dry}+m_{wv}\chi_{wv}(p))g(p)} \quad (11)$$

Thus, the absorption cross-section  $\sigma(\lambda, p(z), T(z))$  is related to atmospheric temperature and pressure, and thus it can be rewritten as  $\sigma(\lambda, p, T(p))$  in pressure  $p$  coordinates. Combining Eq. (11), we can transform Eq. (5) from the elevation  $z$  coordinate to the pressure  $p$  coordinate. The differential optical depth  $dOD$  associated with pressure  $p$  coordinates is expressed by

$$dOD(p_{ground}, p_{top}) = 0.20948 \int_{p_{top}}^{p_{ground}} \frac{\Delta\sigma(v, p, T(p))}{(m_{dry}+m_{wv}\chi_{wv}(p))g(p)} dp \quad (12)$$

Here we assume that the pressure at the top of the atmosphere is  $p_{top}=0.0$ , and the atmospheric pressure at the surface (or cloud top)  $p_{ground}=p_{surface}$ .

$$dOD(p_{surface}) = \frac{0.20948}{g} \int_0^{p_{surface}} \frac{\sigma(v_{on}, p, T(p)) - \sigma(v_{off}, p, T(p))}{m_{dry}+m_{wv}\chi_{wv}(p)} dp \quad (13)$$

Equation (13) establishes the implicit expression of the differential optical depth of the entire aerosphere with respect to the surface pressure  $p_{surface}$ . Theoretically, the true value of the differential optical depth is the state of the atmosphere and is not related to the LIDAR parameters. Further, it is independent of the measurement method. However, the measurement error of the differential optical depth is closely related to the LIDAR parameters. In the pressure  $p$  coordinate, the differential optical depth  $dOD(p_{surface})$  is expressed through the integral Eq. (14) as follows:

$$dOD(p_{surface}) = \int_0^{p_{surface}} \frac{\sigma(v_{on}, p, T(p)) - \sigma(v_{off}, p, T(p))}{2.251667 \times 10^{-24} \times (1 + 0.6214 \chi_{wv}(p))} dp \quad (14)$$



On differentiating both sides of Eq. (13) with respect to  $p_{surface}$  and considering the derivative function of  $dOD(p_{surface})$  with respect to  $p_{surface}$ , we obtain

$$\frac{\partial(dOD(p_{surface}))}{\partial p_{surface}} = \frac{1}{46.8119} \times \frac{\sigma(v_{on,p_{surface},T(p_{surface})) - \sigma(v_{off,p_{surface},T(p_{surface}))}{m_{dry} + m_{wv}\chi_{wv}(p_{surface})} \quad (15)$$

Subsequently, the relationship between the errors of the surface pressure and the differential optical depth of the entire atmosphere is obtained as

$$\delta p_{surface} = \frac{46.8119 \times [m_{dry} + m_{wv}\chi_{wv}(p_{surface})]}{\sigma(v_{on,p_{surface},T(p_{surface})) - \sigma(v_{off,p_{surface},T(p_{surface}))} \delta[dOD(p_{surface})] \quad (16)$$

Assuming that the vertical profile of atmospheric temperature  $T(R)$  and the vertical profile of water vapor mixing ratio  $\chi_{wv}(R)$  are known from data obtained from other sensors or weather models, the surface pressure can be inverted from the differential optical depth of the entire atmosphere. The steps are shown in Fig. 1.

a. The differential optical depth measurement value  $(dOD)_m$  of the atmosphere from the echo signal  $N_s$  and emission energy  $E$  of the differential absorption LIDAR is calculated.

b. Utilizing the atmospheric temperature profile  $T(R)$  coupled with the pressure profile and the surface pressure in the standard atmosphere mode as the initial value of the atmospheric pressure profile  $p_1(R)$  and the initial value of the surface pressure  $p_{surface,1}$ , respectively, and using the oxygen HITRAN database, the initial value of the absorption coefficient profile of the entire atmosphere is calculated. Thereafter, the initial value of the differential optical depth  $(dOD)_{c,1}$  of the entire atmosphere is calculated.

c. If the differential optical depth  $(dOD)_{c,i}$  of the entire atmosphere is numerically calculated in  $i$ -th cycle and  $(dOD)_{c,i}$  is not equal to the differential optical depth  $(dOD)_m$  measured by the LIDAR, then the surface pressure  $p_{surface,i}$  calculated using the numerical value is not equal to the true value  $p_{surface}$  of the pressure at the footprint, and thus,  $(dOD)_m$  is subtracted from  $(dOD)_{c,i}$ .

d. The surface pressure varies with the differential optical depth. In the  $i$ -th cycle, the difference between  $(dOD)_{c,i}$  and  $(dOD)_m$  is multiplied by a coefficient

$$\frac{46.8119 \times [m_{dry} + m_{wv}\chi_{wv}(p_{surface,i})]}{\sigma(v_{on,p_{surface,i},T(p_{surface,i})) - \sigma(v_{off,p_{surface,i},T(p_{surface,i}))}$$

in Eq. (16) as the compensation amount and added to the calculated value of the surface pressure  $p_{surface,i}$ . Consequently, the resulting sum is used as the new surface pressure  $p_{surface,i+1}$ ;  $p_{surface,i+1} = p_{surface,i} +$

$$\frac{46.8119 \times [m_{dry} + m_{wv}\chi_{wv}(p_{surface,i})]}{\sigma(v_{on,p_{surface,i},T(p_{surface,i})) - \sigma(v_{off,p_{surface,i},T(p_{surface,i}))} (dOD_{c,i} - dOD_m).$$

e. Subsequently, with atmospheric temperature profile  $T(R)$  and water vapor mixing ratio  $\chi_{wv}(R)$  provided by other sensors or numerical weather models, coupled with the surface pressure result  $p_{surface,i}$  obtained in the  $i+1$ -th cycle, the atmospheric pressure profile  $p_{i+1}(R)$

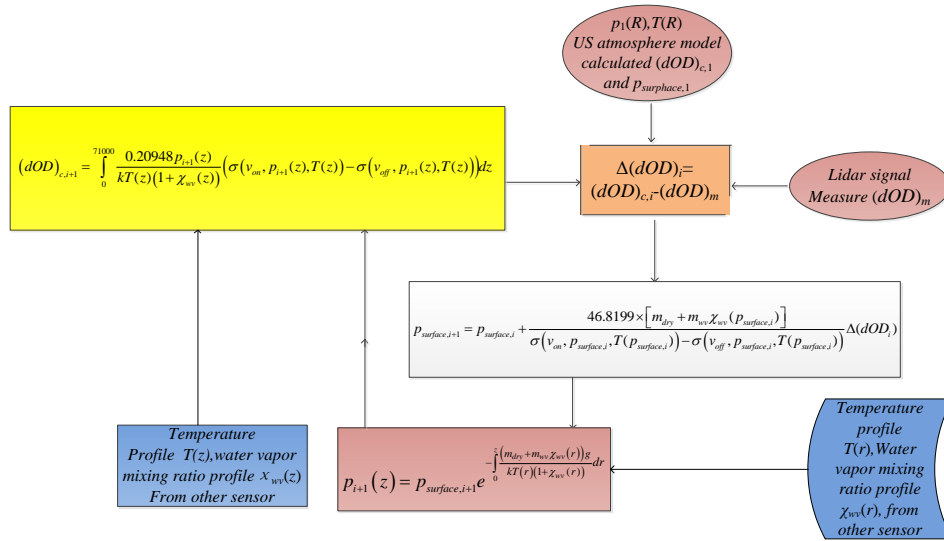
$$\text{is calculated, } p_{i+1}(R) = p_{surface,i} \cdot \exp^{-\int_0^R \frac{m_{dry} + m_{wv}\chi_{wv}(z)}{kT(z)(1 + \chi_{wv}(z))} g(z) dz}.$$

f. Further, with the atmospheric temperature profile  $T(R)$ , profile for water vapor mixing ratio  $\chi_{wv}(R)$ , and the atmospheric pressure profile  $p_{i+1}(R)$ , based on the HITRAN database, differential optical depth  $(dOD)_{c,i+1}$  calculations are repeated.

g. Repeat steps c–f. In the case of the above iterative process, with increase in  $i$ , the difference between  $(dOD)_{c,i}$  and  $(dOD)_m$  decreases till  $i=M$ ,  $p_{surface, M+1} - p_{surface, M}$  is comparable to the error. If that happens, the iterative loop stops. Herein, the output surface pressure  $p_{surface, M}$  calculation result is considered to be sufficiently close to the true value  $p_{surface}$ .



The above calculation steps also suggest that the parameters related to the temperature, pressure, and humidity of the atmosphere should be detected synchronously in the future, as input conditions for each other, and simultaneously iterated.



219  
220

Figure 1: Iterative calculation process of the atmospheric pressure on the surface of the differential optical depth measured by the differential absorption LIDAR.

### 3 Performance evaluation of an integrated path differential absorption LIDAR model

#### 3.1 A-band absorption spectrum of Oxygen

The absorption line of oxygen molecules is broadened in the atmosphere via collision and Doppler broadening. They are expressed via the famous Lorentz and Gauss line shapes, respectively. Below 15km in the atmosphere, collision broadening is dominant, with “n” representing the sensitivity factor of collision broadening with respect to air temperature, that is, the average value of its own broadening and nitrogen broadening sensitivity factors. We consider  $n=0.73-0.59$  from HITRAN database, normal pressure  $p_0=1013.25\text{hPa}$ , normal temperature  $T_0=296\text{K}$ ,  $\gamma_0$  is the pressure broadening under normal temperature and normal pressure,  $S_0$  is the intensity of the absorption line at room temperature and pressure,  $\sigma_0$  is the peak absorption cross section of the absorption line at room temperature and pressure,  $c$  is the speed of light,  $h$  is the Planck constant,  $m$  is the molecular mass of oxygen, and  $\nu_0(\text{cm}^{-1})$  represents the position of the center wave number (light frequency) of the absorption line. Further,  $E''$  is the energy of the low-energy state of the electron. Moreover, in the application of differential absorption LIDAR, the absorption line shape of the oxygen molecule can be represented using the Voigt line shape, which is a form of the convolution Gauss line shape with Lorentz line shape. The arbitrary real number  $t$  is the variable of the Voigt linear integral.

The absorption cross-section  $\sigma(\nu)$  at the light wave number  $\nu$  is written as  $\sigma(\nu) = \sigma_0 \frac{y}{\pi} \int_{-\infty}^{\infty} \frac{\exp(-t^2)}{y^2 + (x-t)^2} dt$ , where  $x = \left(\frac{\nu - \nu_0}{\nu_0}\right) \left(\frac{m}{2kT}\right)^{0.5} c$  and  $y = \nu_0 \gamma_0 \left(\frac{p}{p_0}\right) \left(\frac{T_0}{T}\right)^n \left(\frac{m}{2kT}\right)^{0.5} c$ , and

$\sigma_0 = \frac{S_0 c}{\nu_0} \left(\frac{2\pi kT}{m}\right)^{0.5} \left(\frac{T_0}{T}\right)^{1.5} \exp\left[\frac{E'' c}{k} \left(\frac{1}{T_0} - \frac{1}{T}\right)\right]$ . The wavelength in the trough between the oxygen absorption line P13Q12 and P13P13, between the oxygen absorption line P15P15 and P15Q14, and even absorption lines P17Q16 and P17P17 can be selected as the detection

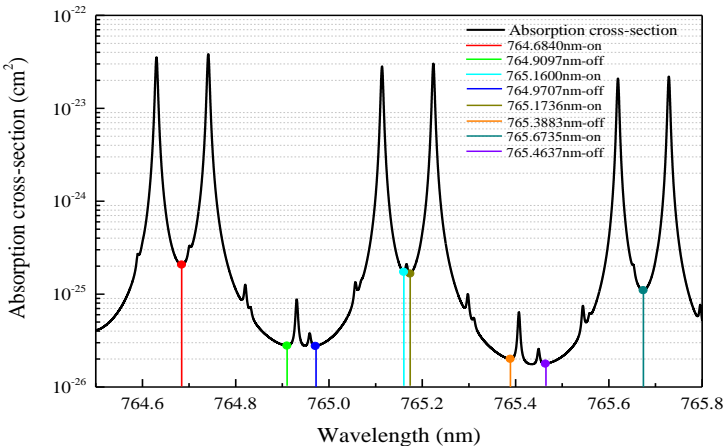
241  
242  
243  
244



wavelength. Table 1 lists certain parameters of the six absorption lines: for example, the linear function  $\sigma_q(v-v_{01})$  of the absorption cross-section of the oxygen absorption line P13Q12 with respect to the wave number  $v$ , and the line function  $\sigma_p(v-v_{02})$  of the absorption cross-section of the P13P13 with respect to the wave number  $v$ . Further, the wavelength  $\lambda_{on}$  (wavenumber  $v_{on}$ ) we selected is located at the minimum of the absorption cross-section between the two spectral lines, that is, its absorption cross-section is the superposition of the values of the extension lines of two adjacent Voigt linear functions at  $v_{on}$ . Moreover, its absorption cross-section  $\sigma_{on}(v)=\sigma_p(v_{on})+\sigma_q(v_{on})$ —the wings of the two Voigt lineshape functions—is the manifestation of their pressure expansion.

**Table 1 Parameters of the three groups of absorption lines of Oxygen A(296K) (Brown and Plymate, 2014)**

Assignment	Line center	Intensity	Low energy	Half Widths		Pressure-introduced shift	Temperature dependence
	$v_0$	$S_0$	$E''$	$\gamma_0$		Average( $\delta$ )	$n$
	$\text{cm}^{-1}$	$\text{cm mole}^{-1}$	$\text{cm}^{-1}$	$\gamma_{\text{air}}$	$\gamma_{\text{self}}$	$\text{cm}^{-1}/\text{atm}$	
P13Q12	13078.2275	$5.61 \times 10^{-24}$	260.6824	0.0466 (0.6)	0.0461 (1.1)	-0.0061	0.73
P13P13	13076.3273	$6.13 \times 10^{-24}$	262.5827	0.0467 (0.8)	0.0460 (1.1)	-0.0068	0.73
P15Q14	13069.9619	$4.33 \times 10^{-24}$	343.9694	0.0457 (1.2)	0.0449 (1.6)	-0.0051	0.73
P15P15	13068.0818	$4.68 \times 10^{-24}$	345.8495	0.0455 (1.2)	0.0452 (1.6)	-0.0064	0.73
P17Q16	13061.3273	$3.09 \times 10^{-24}$	438.7010	0.044	0.045	-0.00898	0.73
P17P17	13059.4665	$3.31 \times 10^{-24}$	440.5618	0.0452	0.045	-0.00902	0.59



(a)

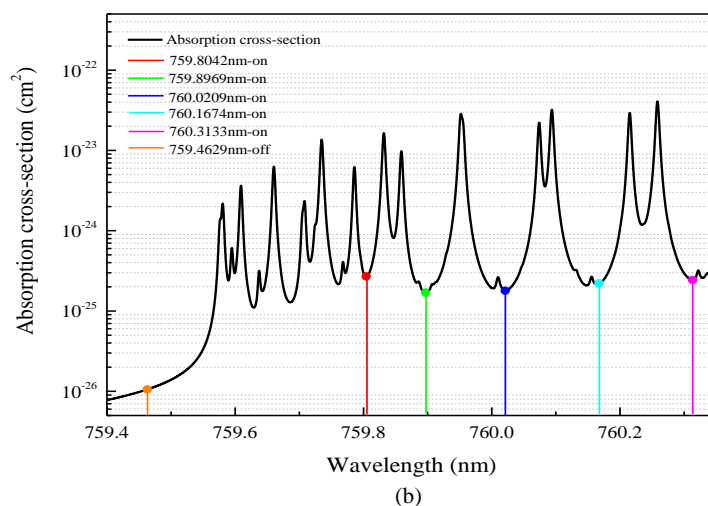
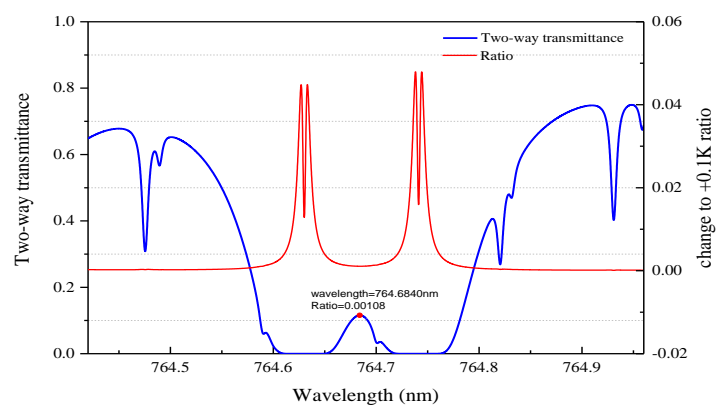
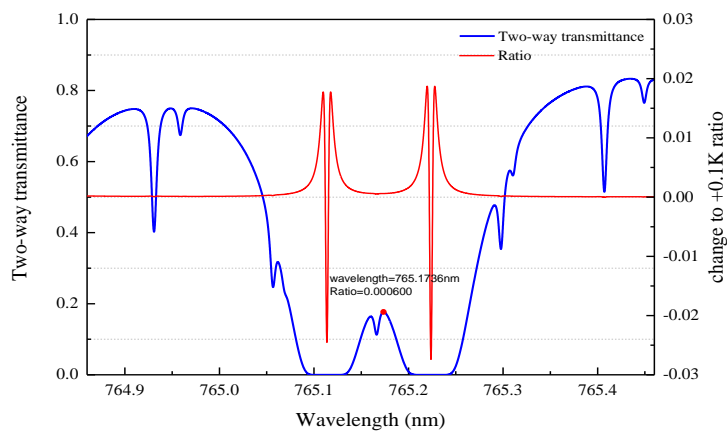


**Figure 2:** (a) Near-ground absorption cross-section near 765nm, (b) Near-ground absorption cross-section near 760nm

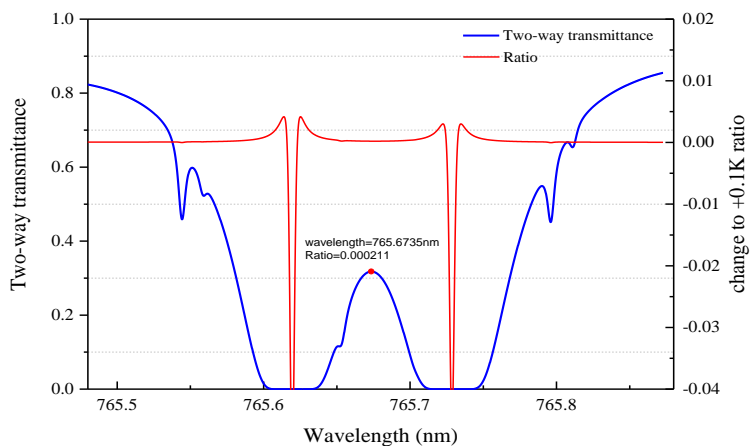
Within the A absorption band of oxygen (759–770nm), the spectral transmittances in the vicinity of 760 and 765nm were relatively insensitive to temperature, this band is the low interference of water vapor and carbon dioxide molecules. Further, the atmospheric transmittance at 760nm is lower than the atmospheric transmittance at 765nm, and when ground-based LIDAR (RR-DIAL) detects tropospheric backscattering owing to the round-trip optical path being shorter, two adjacent lines near 760nm can be selected. In addition, the plots of absorption spectra shown in Figure 2, the Oxygen absorption features with a number of smaller and sharper absorption spikes, it contains isotopologues of Oxygen molecules, showing some subtle differences, the wavelength in the middle of the trough area between lines is more suitable as the detection wavelength online and the reference wavelength offline (Korb et al., 1983, 1989; Schwemmer, et al., 1987). When IPDA shoots lasers from the satellite and receives the echo from the ground surface, the laser beam that passes through the entire atmosphere twice results in the path being longer. Thus, 765nm is relatively more suitable for remote sensing of surface pressure from satellites (Riris et al., 2017).



276



277



278

279

280

**Figure 3:** Transmittance spectra of three intervals around 765nm and their ratio to 0.1K change in temperature

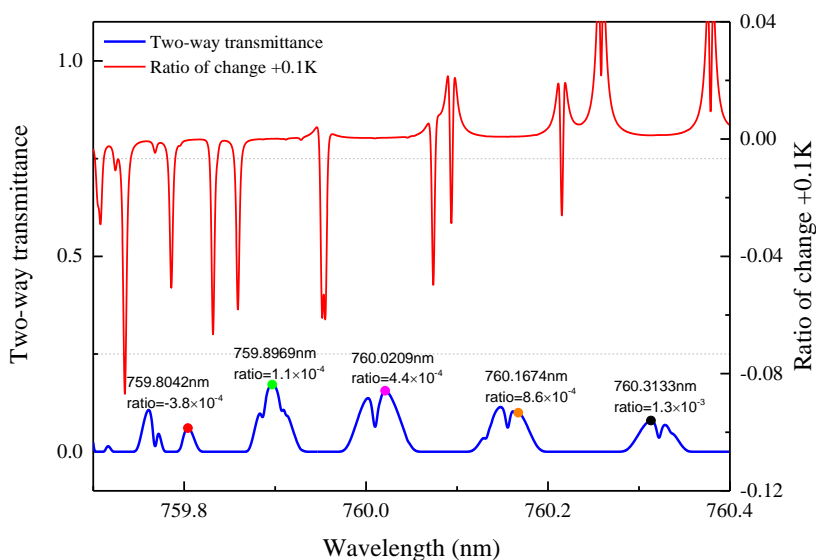


**Figure 4:** Transmittance spectra around 760nm and their ratio to 0.1K change in temperature

The absorptive optical depth of oxygen  $dOD(p_{surface})$  with respect to the path 0–71km corresponds to the optical transmittance  $e^{-2dOD}$  of this path with respect to the  $\nu$  wavenumber. Figure 3 shows the transmittance spectra of three intervals around 765nm and their sensitivity to temperature changes of +0.1K. Similarly, Figure 4 shows the transmittance spectra of around 760nm and their sensitivity to temperature changes of +0.1K.

**Table 2 differential optical depth and differential absorption cross section of 9 pairs of wavelengths in standard atmospheric mode**

Wavelength(nm)	$\int_0^{71} (\alpha_m + \alpha_a) dz$	$\int_0^{71} (n_{O_2} \sigma) dz$	$OD(0,71km)$	$\sigma_{O_2} (cm^2)$	$dOD(0,71km)$	$\Delta\sigma_{O_2} (cm^2)$
on 764.6840	0.1852	0.493	0.678	$2.08 \times 10^{-25}$	0.428	$1.80 \times 10^{-25}$
off 764.9097	0.1851	0.0653	0.251	$2.80 \times 10^{-26}$		
on 765.1600	0.1851	0.389	0.574	$1.74 \times 10^{-25}$	0.325	$1.46 \times 10^{-25}$
off 764.9707	0.1851	0.0638	0.249	$2.77 \times 10^{-26}$		
on 765.1736	0.1849	0.373	0.558	$1.67 \times 10^{-25}$	0.328	$1.47 \times 10^{-25}$
off 765.3883	0.1849	0.0448	0.230	$2.01 \times 10^{-26}$		



on	765.6735	0.1848	0.231	0.416	$1.10 \times 10^{-25}$	0.192	$9.25 \times 10^{-26}$
off	765.4637	0.1849	0.0391	0.224	$1.78 \times 10^{-26}$		
on	759.8042	0.1872	0.515	0.702	$2.60 \times 10^{-25}$	0.493	$2.49 \times 10^{-25}$
off	759.4629	0.1873	0.0216	0.209	$1.46 \times 10^{-26}$		
on	759.8969	0.1871	0.343	0.530	$1.66 \times 10^{-25}$	0.321	$1.55 \times 10^{-25}$
off	759.4629	0.1873	0.0216	0.209	$1.46 \times 10^{-26}$		
on	760.0209	0.1871	0.385	0.573	$1.77 \times 10^{-25}$	0.364	$1.67 \times 10^{-25}$
off	759.4629	0.1873	0.0216	0.209	$1.46 \times 10^{-26}$		
on	760.1674	0.1870	0.506	0.693	$2.22 \times 10^{-25}$	0.484	$2.12 \times 10^{-25}$
off	759.4629	0.1873	0.0216	0.209	$1.46 \times 10^{-26}$		
on	760.3133	0.1870	0.576	0.763	$2.46 \times 10^{-25}$	0.554	$2.36 \times 10^{-25}$
off	759.4629	0.1873	0.0216	0.209	$1.46 \times 10^{-26}$		

292

293 Equation (16) clearly indicates that in various factors that result in  $\delta[dOD(p_{\text{surface}})]$ , the error  
 294 of differential optical depth conditionally causes the error  $\delta p_{\text{surface}}$  of the  
 295 surface pressure. Additionally, the detection wavelength absorption cross-section difference  
 296  $\Delta\sigma(p_{\text{surface}})$  near the ground is inversely proportional to the surface pressure error. Evidently, a  
 297 key factor affecting DIAL sensitivity is the online and offline wavelength positions. However,  
 298 for the candidate wavelengths marked in Fig. 2 used as detection wavelengths, each would  
 299 offer its own advantages and disadvantages, and consequently, comprehensive evaluation is  
 300 required.

### 301 3.2 Differential absorption LIDAR system model

302 The research results reported by Coney, *et al.*(Munk et al., 2016-2019; Coney et al., 2021;  
 303 Thomas et al., 2016; Strotkamp et al., 2019)along with those reported by Wulfmeyer  
 304 and  osenberg et al.(1996), refer to the ADM-Aeolus in orbit ALADIN system parameters of  
 305 the Aeolus mission (Lemmerz et al., 2017); the receiver is based on the GLAS-Mission-  
 306 1064nm receiver, the orbit altitude is 400km, and diameter of the telescope is 1.5m.  
 307 Consequently, the model parameters of the differential absorption LIDAR has been proposed,  
 308 as shown in Table 3. The transmitter model parameters, with the exception of the pulse  
 309 energy of 100mJ, have been separately reported in different documents(Coney et al.,  
 310 2021).However, these indicators have been achieved in the same laser, and thus, more  
 311 research is required.

312

Table 3 System parameters of differential absorption LIDAR

Transmitter	
Laser pulse energy	100mJ



Laser pulse Width	88ns
Pulse repetition rate	100Hz
Laser Divergence Angle	90μrad for ±3σ
Spectral purity	99.99%
Pointing stability	< 10μrad
Receiver	
Telescope Diameter ( $A_t$ )	1.5m(SiC)
Receiver Field-of-view (full)	100μrad
Optical Filter Bandwidth ( $FW$ )	0.8nm(FWHM)
Fabry-Perot Elton (thickness=2mm)	25pm(free spectral range ≈ 0.1nm)
Receiver Efficiency	50%
Combined filter width	0.025nm
Detector and amplifier	
Detector(Laser Components DG, Inc)	Si-APD(SAR1500/C30956/S3884-04)
APD Quantum Efficiency ( $\eta_d$ )	75%
Detector Diameter	Φ1.5mm
Electronic system bandwidth ( $BW$ )	3MHz
APD dark current ( $I_d$ )	1nA type
APD gain( $M$ )	100
APD excess noise factor( $F$ )	2.4
APD capacitance ( $C_d$ )	4pF
trans-impedance amplifier gain ( $R_f$ )	20kV/A
trans-impedance amplifier input current noise ( $I_{nA}$ )	2.5pA/Hz <sup>1/2</sup>
trans-impedance amplifier input voltage noise ( $V_{nA}$ )	20nV/Hz <sup>1/2</sup>
operate temperature	293 K
Platform and environment	
Orbit altitude and velocity	400 km, 7 km/s
Orbit type	Polar, sun synchronous, dawn/dusk
Along-track resolution	44 km
Simulation top altitude	71 km
Viewing geometry	Nadir
Atmosphere model	US standard atmosphere
Aerosol model	Median aerosol profile
(765nm)the surface albedo over ocean/land	0.1575/0.314
Pointing stability	< 50μrad
Spectroscopic data base	HITRAN 2012

As reported in reference (Lancaster et al., 2005), the equivalent Lambertian reflection coefficient of the sub-satellite point laser on the ocean surface has an empirical relationship  $\rho_{eff} = \frac{\rho}{4\langle S^2 \rangle}$ , where the Fresnel reflection coefficient is  $\rho = 0.02$ , and  $\langle S^2 \rangle$  is the variance of the wave steepness distribution. Further, Bufton et al.(1983)and Menzies et al.(1998)individually adopted relationship as follows:



$$\langle S^2 \rangle = \begin{cases} (\ln U_{10} + 1.2) \times 10^{-2} \\ (0.85 \ln U_{10} - 1.45) \times 10^{-1} \end{cases} \quad U_{10} \leq 7.0 \text{ m/s} \quad U_{10} > 7.0 \text{ m/s} \quad (17)$$

where  $U_{10}$  is the wind speed of segment 10m above the ocean surface. The general ocean surface wind speed is taken as 8m/s, whereas  $\rho_{\text{eff}} = 0.1575$  and  $\rho_{\text{eff}}\pi = 0.025 \text{ sr}^{-1}$ . In addition, the reflectivity of terrestrial lasers is generally 0.314.

### 3.3 Performance evaluation of A-band DIAL system

#### 3.3.1 Random error of differential optical depth caused by noise

The number of received return echo photons  $N_{s,\text{on}}$  and  $N_{s,\text{off}}$  is obtained using the LIDAR Eq. (7) and Eq.(8). Equations(18)–(25) are commonly used for the on and off channels.

$$N_s(R_0, R) = \frac{\lambda \cdot E}{h \cdot c} \cdot A_r \cdot \eta_d \cdot \eta_r \cdot \left( \frac{\rho}{\pi} \right) \cdot \frac{\exp[-2OD(R_0, R)]}{(R_0 - R)^2} \quad (18)$$

Here the working and reference wavelengths  $\lambda_{\text{on}}$  and  $\lambda_{\text{off}}$ , the Planck constant is  $h$ ,  $\rho$  is the surface reflectivity, and  $c$  is the speed of light. Further, the effective pulse width  $\tau_w$  of the echo signal is a combination of the emitted laser pulse width  $\tau_L$ , and the detection electronic system bandwidth  $BW$  (unit Hz), effective target altitude within the laser footprint  $\Delta H$ ,  $R_0=400\text{km}$ ,  $\Delta H=2$  m, can be expressed as (Ehret, et al., 2008):

$$\tau_w = \sqrt{\tau_L^2 + \left( \frac{1}{3} \cdot BW \right)^2 + \left( \frac{2 \cdot \Delta H}{c} \right)^2} \quad (19)$$

The background signal  $N_{BG}$  (photoelectrons), assuming a Lambertian surface and zenith sun, is calculated as

$$N_{BG}(\lambda) = \frac{\lambda \cdot S_{BG}}{h \cdot c} \tau_w \cdot A_r \cdot \eta_d \cdot \eta_r \cdot \left( \frac{\rho}{\pi} \right) \cdot \left( \frac{FOV}{2} \right)^2 \pi \cdot FW \cdot \exp[-2OD(R_0, R)] \quad (20)$$

where  $S_{BG}$  is the exo-atmospheric solar irradiance value ( $1.221 \text{ W m}^{-2} \text{ nm}^{-1}$ ) (ASTM international, United States, 2019) at 765nm,  $FW$  is the bandwidth of the optical filter ( $0.025 \text{ nm} \times 4$ ) and the field of view (FOV) (unit rad) of the  $FOV$  receiving telescope. The bandwidth of the Fabry–Perot etalon, free spectral range, and width of the narrowband filter were 25pm, 0.1nm, and 0.8nm, respectively. There are 8 longitudinal modes of Fabry–Perot etalon that can pass through. However, the transmittance of each longitudinal mode is different, and thus, the equivalent solar window width is  $25 \text{ pm} \times 4 = 0.1 \text{ nm}$ . Further, the backscattering coefficient ( $\rho/\pi$ ) on the surface of land such as ocean and vegetation during the daytime (Thomas et al., 2016), and  $\rho$  were calculated as 0.1575 and 0.314, respectively.

Here the  $q$  electrons charge is  $1.6 \times 10^{-19} \text{ C}$ ,  $M$  is the gain of silicon avalanche diode (APD). The total noise associated with the detection signal is divided into fixed circuit noise and signal-dependent shot noise. The total circuit noise current spectral density (unit  $\text{A/Hz}^{1/2}$ )  $I_n$ , can be expressed as (Refaat, et al., 2013)

$$I_n = \sqrt{2 \cdot q \cdot I_d \cdot M \cdot F + I_{nA}^2 + \frac{V_{nA}^2}{R_f^2} + \frac{4 \cdot k \cdot T}{R_f + \frac{(2 \cdot \pi \cdot V_{nA} \cdot C_d \cdot BW)^2}{3}}} \quad (21)$$

where  $I_d$  and  $F$  are the dark current and excess noise factors of the detector, respectively;  $I_{nA}$  and  $V_{nA}$  are the preamplifier integrated input current and input voltage noise spectral density, respectively;  $R_f$  is the feedback resistance of the preamplifier; and  $C_d$  is the equivalent input capacitance of the amplifier and the detector. The circuit noise is often limited by the shot noise of the dark current of the detector or the noise of the preamplifier. In this analysis, all circuit noises refer to the detector input and the equivalent circuit noise-generated photoelectrons, and  $N_{n,C}$ , is calculated as



$$N_{n,C} = \frac{I_n \cdot \tau_w \cdot \sqrt{BW}}{q \cdot M} \quad (22)$$

Similarly, the equivalent shot noise-generated photoelectrons,  $N_{n,S}$ , are calculated as

$$N_{n,S} = \sqrt{2 \cdot N_S \cdot F \cdot \tau_w \cdot BW} \quad (23)$$

Further, the photoelectron  $N_{n,BG}$ , equivalent to the equivalent shot noise associated with the background radiation can be calculated as

$$N_{n,BG} = \sqrt{2 \cdot N_{BG} \cdot F \cdot \tau_w \cdot BW} \quad (24)$$

These noises are regarded as the equivalent photoelectron number generated in the detector (before the multiplication process), and are proportional to the actual detected photoelectron number. The total signal-to-noise ratio is expressed as follows (Ehret, *et al.*, 2008):

$$SNR_{on/off} = \frac{N_{s,on/off}}{\sqrt{N_{n,C}^2 + N_{n,S,on/off}^2 + N_{n,BG,on/off}^2}} \quad (25)$$

Where  $s$  is the number of echo signal pulses accumulated and averaged by the LIDAR. The error  $\varepsilon_R$  caused by the noise of the LIDAR receiving a single echo is a random error. Moreover, it is necessary to calibrate the LIDAR echo signal detection channel and the laser emission pulse energy monitoring channel to remove nonlinear and nonzero biased background voltage. Further, the calibration error and AD conversion error comprise the systematic error. In addition, the error  $\varepsilon_A$  caused by the uncertainty of atmospheric environment (atmospheric temperature profile, atmospheric water vapor mixing ratio profile), and the associated error  $\varepsilon_T$  of the laser emission characteristics (jitter of the center wavelength of the emitted beam, the emission spectrum width, and the purity of the emission spectrum) are all systematic errors. The total error of the differential optical depth can be expressed as

$$\delta[dOD] = \frac{\varepsilon_R}{\sqrt{s}} + \sqrt{\varepsilon_A^2 + \varepsilon_T^2} \quad (26)$$

Equation(9) indicates that the random noise of the echo signals  $N_{on}(R)$  and  $N_{off}(R)$  and the random measurement error of the pulse energies  $E_{on}$  and  $E_{off}$  result in the random error of the differential optical depth  $\varepsilon_R = \delta[dOD(p_{surface})]_R$  as follows:

$$\varepsilon_R = \delta[dOD(p_{surface})]_R = \frac{1}{2} \sqrt{\left(\frac{\delta N_{s,on}(R)}{N_{s,on}(R)}\right)^2 + \left(\frac{\delta N_{s,off}(R)}{N_{s,off}(R)}\right)^2 + \left(\frac{\Delta E_{on}}{E_{on}}\right)^2 + \left(\frac{\Delta E_{off}}{E_{off}}\right)^2} \quad (27)$$

The signal-to-noise ratio of LIDAR can be calculated using Eq.(18)–(25). Simultaneously, it is considered that the measurement error of pulse energy  $\Delta E_{on}/E_{on} \approx \Delta E_{off}/E_{off}$  is very small and can thus be ignored. The random error of LIDAR echo (noise) measurement is calculated as

$$\varepsilon_R = \frac{1}{2} \sqrt{SNR_{on}^{-2} + SNR_{off}^{-2}} \quad (28)$$

When the laser irradiates the ocean surface (for example, the average wind speed is 8m/s), 0.1575 represents median for the ocean surface reflectivity (Ehret, *et al.*, 2008), and the random error  $\varepsilon_R$  of the differential optical depth is calculated considering the single pulse echo; with a time resolution of at least 6.25 s, the distance resolution along the track of 44km and  $S = 625$  laser pulse echoes are taken as a group for cumulative average, the random error of the atmospheric differential optical depth above the ocean surface is  $\frac{\varepsilon_R}{\sqrt{625}}$ .

The ocean surface possesses low laser reflectivity and weak echoes. The averaging method employed is as follows: first add up 625 echoes; thereafter subtract  $B$  and normalize,



where  $B$  is the level background baseline of the LIDAR output; and finally Eq. (25) provides the differential optical depth.

$$E_{on} = \sum_{i=1}^{625} E_{i,on} \quad (29-1)$$

$$E_{off} = \sum_{i=1}^{625} E_{i,off} \quad (29-2)$$

$$N_{s,on} = \sum_{i=1}^{625} N_{i,s,on} \quad (29-3)$$

$$N_{s,off} = \sum_{i=1}^{625} N_{i,s,off} \quad (29-4)$$

$$dOD = OD_{on} - OD_{off} = -\frac{1}{2} \ln \left( \frac{N_{s,on} - B}{E_{on}} \right) + \frac{1}{2} \ln \left( \frac{N_{s,off} - B}{E_{off}} \right) \quad (30)$$

**Table 4 Error from noise**

Wavelength (nm)	SNR		Single shot Noise Error		average Noise Error	
	ocean	land	ocean	land	Ocean/25	Land/12
	0.1575	0.314	0.1575	0.314	0.1575	0.314
764.6840	97.74	139.68	0.0061	0.0043	$2.44 \times 10^{-4}$	$3.55 \times 10^{-4}$
764.9097	152.1	215.8				
765.1600	109.0	155.5	0.0056	0.0040	$2.24 \times 10^{-4}$	$3.30 \times 10^{-4}$
764.9707	152.3	216.2				
765.1736	110.9	158.0	0.0055	0.0039	$2.20 \times 10^{-4}$	$3.24 \times 10^{-4}$
765.3883	155.4	220.5				
765.6735	128.4	182.6	0.0050	0.0035	$2.00 \times 10^{-4}$	$2.96 \times 10^{-4}$
765.4637	156.3	221.8				
759.8042	95.06	135.9	0.00614	0.00430	$2.46 \times 10^{-4}$	$3.58 \times 10^{-4}$
759.4629	158.1	224.3				
759.8969	113.7	161.9	0.00542	0.00381	$2.17 \times 10^{-4}$	$3.17 \times 10^{-4}$
759.4629	158.1	224.3				
760.0209	108.8	155.1	0.00558	0.00392	$2.23 \times 10^{-4}$	$3.27 \times 10^{-4}$
759.4629	158.1	224.3				
760.1674	95.98	137.2	0.00609	0.00427	$2.44 \times 10^{-4}$	$3.56 \times 10^{-4}$
759.4629	158.1	224.3				



760.3133	89.15	127.7				
759.4629	158.1	224.3	0.00644	0.00451	$2.58 \times 10^{-4}$	$3.76 \times 10^{-4}$

404

405 It is believed that the reflectance value of 0.314 is typical and representative of the surface  
 406 reflectance for most features on land (vegetation, sand, and soil). When the laser irradiates the  
 407 land, the noise of the single pulse echo causes a random error in the optical depth. The time  
 408 resolution of 6.25 s and resolution along track of 44 km are maintained. First, the very high  
 409 footprint is highlighted, and the very low footprint points is removed. Subsequently, the  
 410 average altitude of most of the remaining footprints is calculated. Considering this average  
 411 altitude, all the echo pulses whose footprint altitude and the average altitude are within 2 m as  
 412 a group are acquired, and the number of pulses obtained is no less than 144 pulses. Further,  
 413 they are accumulated and averaged to decrease the random measurement error of the  
 414 differential optical depth.

415 The averaging method involves first subtracting the background baseline  $B_i$  of a single  
 416 echo, normalizing, and thereafter performing the cumulative average, where

$$417 \quad s \geq 144, \quad \frac{N_{s,on/off}}{E_{on/off}} \approx \sum_{i=1}^M \frac{N_{i,s,on/off} - B_i}{E_{i,on/off}} \quad (31)$$

$$418 \quad dOD = OD_{on} - OD_{off} = -\frac{1}{2} \ln \left( \frac{N_{s,on}}{E_{on}} \right) + \frac{1}{2} \ln \left( \frac{N_{s,off}}{E_{off}} \right) \quad (32)$$

419 When the laser irradiates the plain area, it is easy to confidently pick out the footprint altitude  
 420 of more than 144 shots from 625 pulses. However, if uneven terrain is encountered, there are  
 421 less than 144 echo pulses, difference between the footprint altitude and the average altitude is  
 422 within 2 m, and average of multiple laser pulse echoes becomes unreasonable. Moreover, if  
 423 greater than 144 pulses with similar footprints are still not found, this set of data is discarded.

424 In conclusion, when laser irradiates the ocean surface, its single echo signal is relatively  
 425 weak, whereas its footprint altitude is relatively consistent; thus, more pulse echoes can be  
 426 accumulated and averaged. Further, when the laser irradiates the land surface, the altitude  
 427 consistency of the landing footprint is poor and accumulated average echo pulse is less,  
 428 although the signal-to-noise ratio of the land single echo is relatively high.

429

### 430 3.3.2 Uncertainty of vertical distribution profile of atmospheric temperature

431 Within a certain time resolution (distance resolution), the uncertainty of the vertical profile of  
 432 the atmospheric temperature results in an absolute systematic error with respect to the  
 433 differential optical depth (Refaat, et al., 2013).

434 When the temperature change  $\pm 1K$ , Oxygen number density is

$$435 \quad n_{O_2}(T \pm 1K) = \frac{0.20948p(z)}{k(T(z) \pm 1) \cdot (1 + \chi(z))} \quad (33)$$

$$436 \quad \Delta[dOD(0, surface)]_{\pm 1K} = \int_0^{71} n_{O_2}(T \pm 1K) \Delta\sigma(p(z), T(z) \pm 1) dz \\ - \int_0^{71} n_{O_2}(T) \Delta\sigma(p(z), T(z)) dz \quad (34)$$

437

Table 5 Temperature sensitivity of differential optical depth in case of  $\pm 1K$  uncertainty

Regimentation	$\Delta[dOD(p, T - 1)]$	$\Delta[dOD(p, T + 1)]$	$Max\{\Delta[dC - 1], \Delta[d - +1]\}$
---------------	-------------------------	-------------------------	---



764.6840/ 764.9097	0.00216	0.00215	0.00216
765.1600/ 764.9707	0.000929	0.000933	0.000933
765.1736/ 765.3883	0.00102	0.00102	0.00102
765.6735/ 765.4637	0.000139	0.000146	0.000146
759.8042/ 759.4629	0.00141	0.00139	0.00141
759.8969/ 759.4629	0.000173	0.000162	0.000173
760.0209/ 759.4629	0.000624	0.000631	0.000631
760.1674/ 759.4629	0.00170	0.00170	0.00170
760.3133/ 759.4629	0.00285	0.00284	0.00285

438

### 439 3.3.3 Error of differential optical depth $[dOD(0, p_{surface})]_{wv}$ caused uncertainty of the 440 mixture ratio of water vapor

441 The mixture ratio of near-ground water vapor in standard atmospheric mode is 1.247% higher  
 442 than  $\chi_{wv}(p_{surface})$ .

443 The 20% uncertainty of profile for water vapor mixture ratio introduces uncertainty in  
 444 differential optical depth  $[dOD(0, p_{surface})]_{wv}$ .

$$\Delta[dOD(p_{surface})]_{\pm 20\%wv} \approx 0.20948 \int_0^{71km} \frac{p(z)}{kT(z)(1 + (1 \pm 20\%) \chi(z))} (\sigma(\lambda_{on}, z) - \sigma(\lambda_{off}, z)) dz$$

$$- 0.20948 \int_0^{71km} \frac{p(z)}{kT(z)(1 + \chi(z))} (\sigma(\lambda_{on}, z) - \sigma(\lambda_{off}, z)) dz \quad (35)$$

446 Table 6 Error differential optical depth  $[dOD(0, p_{surface})]_{wv}$  caused uncertainty of the mixture of water vapor

Wavelength(nm)	Differential optical depth error(20%)
764.6840	$5.29 \times 10^{-4}$
764.9097	
765.1600	$4.15 \times 10^{-4}$
764.9707	
765.1736	$4.18 \times 10^{-4}$
765.3883	



447	765.6735	2.53 × 10 <sup>-4</sup>
448	765.4637	
449	759.8042	6.71 × 10 <sup>-4</sup>
450	759.4629	
451	759.8969	4.27 × 10 <sup>-4</sup>
452	759.4629	
453	760.0209	4.71 × 10 <sup>-4</sup>
454	759.4629	
455	760.1674	6.11 × 10 <sup>-4</sup>
456	759.4629	
457	760.3133	6.88 × 10 <sup>-4</sup>
458	759.4629	
459		

### 3.3.4 Error of the differential optical depth caused the difference in the altitude of the inner surface and between the land footprints.

The largest oxygen density is near the ground, and thus, differential optical depth is sensitive to high uncertainty near ground;  $\Delta H=2\text{m}$ .

$$\begin{aligned}
 \Delta[dOD(P_{surface})]_{\Delta H} &\approx \int_0^{71000} n_{O_2}(z)(\sigma(\lambda_{on}, z) - \sigma(\lambda_{off}, z))dz \\
 &\quad - \int_{\pm 2}^{71000} n_{O_2}(z)(\sigma(\lambda_{on}, z) - \sigma(\lambda_{off}, z))dz \\
 &\approx \int_0^{\pm 2} n_{O_2}(z)(\sigma(\lambda_{on}, z) - \sigma(\lambda_{off}, z))dz
 \end{aligned} \tag{36}$$

**Table 7 Differential optical depth error caused by the 2 m altitude difference**

Wavelength	Error [ $dOD$ ]
764.6840	0.4578 × 10 <sup>-4</sup>
764.9097	
765.1600	0.3723 × 10 <sup>-4</sup>
764.9707	
765.1736	0.3737 × 10 <sup>-4</sup>
765.3883	
765.6735	0.2356 × 10 <sup>-4</sup>
765.4637	
759.8042	0.139 × 10 <sup>-4</sup>
759.4629	
759.8969	0.0905 × 10 <sup>-4</sup>
759.4629	
760.0209	0.102 × 10 <sup>-4</sup>
759.4629	



467	760.1674	$0.136 \times 10^{-4}$
468	759.4629	
469	760.3133	$0.156 \times 10^{-4}$
470	759.4629	

### 471 3.3.5 Relative error in calibration for the echo and energy monitoring channels.

472 The absolute error in the differential optical depth is  $dOD \times 0.025\%$  (Ehret, et al., 2008),  
 473 which also belongs to the systematic error.

474 Table 8 Calibration error for echo detection channels and energy monitoring channels  
 475

Wavelength(nm)	$dOD(0, 71\text{km})$	error of $dOD$
764.6840	0.428	$1.07 \times 10^{-4}$
764.9097		
765.1600	0.325	$0.81 \times 10^{-4}$
764.9707		
765.1736	0.328	$0.82 \times 10^{-4}$
765.3883		
765.6735	0.192	$0.48 \times 10^{-4}$
765.4637		
759.8042	0.493	$1.23 \times 10^{-4}$
759.4629		
759.8969	0.321	$0.803 \times 10^{-4}$
759.4629		
760.0209	0.364	$0.910 \times 10^{-4}$
759.4629		
760.1674	0.484	$1.21 \times 10^{-4}$
759.4629		
760.3133	0.554	$1.39 \times 10^{-4}$
759.4629		

476

### 477 3.3.6 Error in optical depth due to the wavelength dependence of aerosol scattering

478 In the standard atmosphere mode, Mie and Rayleigh scatterings of the 765nm or 760nm dual-  
 479 wavelength are similar but not equal. The coefficient  $C$  in Eq. (10) expresses the systematic  
 480 error caused by the difference as follows:

$$481 C = \int_0^{71\text{km}} [\alpha_a(\lambda_{on}, z) + \alpha_m(\lambda_{on}, z)] dz - \int_0^{71\text{km}} [\alpha_a(\lambda_{off}, z) + \alpha_m(\lambda_{off}, z)] dz \quad (37)$$

482 Table 9 Optical depth error caused by the wavelength dependence of the aerosol scattering  
 483  
 484



	Wavelength(nm)	C
485	on 764.6840	$0.90 \times 10^{-4}$
486	off 764.9097	
487	on 765.1600	$0.76 \times 10^{-4}$
488	off 764.9707	
489	on 765.1736	$0.86 \times 10^{-4}$
490	off 765.3883	
491	on 765.6735	$0.84 \times 10^{-4}$
492	off 765.4637	
493	on 759.8042	$1.39 \times 10^{-4}$
494	off 759.4629	
495	on 759.8969	$1.77 \times 10^{-4}$
496	off 759.4629	
497	on 760.0209	$2.28 \times 10^{-4}$
498	off 759.4629	
499	on 760.1674	$2.88 \times 10^{-4}$
500	off 759.4629	
501	on 760.3133	$3.47 \times 10^{-4}$
502	off 759.4629	
503		
504		
505		
506		

507 The errors in aerosol Mie scattering with the wavelength dependence error, spectral width  
 508 error, and spectral purity error, can be eliminated by correction. Wavelength dependence of  
 509 extinction coefficient of aerosol,  $0.0 < k < 2.0$ ,  $k$  is uncertain and varies with the particle size,  
 510 shape and concentration of aerosol, so it will bring systematic error of differential optical  
 511 depth.  
 512

### 513 3.3.7 Error in differential optical depth from the spectral purity of the on/off laser

514 The spectral purity  $\zeta$  of the spaceborne IPDA LIDAR is 99.99% (Wulfmeyer and  osenberg et  
 515 al.1996), which results in an increase in the on-channel echo and the absolute error of the  
 516 optical depth. For a spectral purity of 100%, the relationship between the two on/off channel  
 517 signals is considered to be  $N_{s,on}' = N_{s,off}' e^{-2dOD}$  and  $dOD = -\frac{1}{2} \ln \left( \frac{N_{s,on}'}{N_{s,off}'} \right)$ . However,  
 518 because the spectral purity is not 100%, but it only is  $\zeta$ , the relationship between the two  
 519 channel signals is approximately  $N_{s,on} = N_{s,off} [(1 - \xi) + \xi e^{-2dOD}]$ ,  $\ln \left( \frac{N_{s,on}}{N_{s,off}} \right) =$   
 520  $\ln[(1 - \xi) + \xi e^{-2dOD}]$ , and the spectral purity yield the following error in optical depth:

$$\varepsilon_{\xi} = \frac{1}{2} \ln \left( \frac{N_{s,on}}{N_{s,off}} \right) - \frac{1}{2} \ln \left( \frac{N_{s,on}'}{N_{s,off}'} \right)$$

$$\approx dOD + \frac{1}{2} \ln[1 - \xi(1 - e^{-2dOD})] \quad (38)$$



522

**Table 10 Error in differential optical depth from spectral purity of 99.99%**

Wavelength	$dOD(0, 71\text{km})$	Error (spectral purity of 99.99%)
764.6840	0.428	$6.79 \times 10^{-5}$
764.9097		
765.1600	0.325	$4.60 \times 10^{-5}$
764.9707		
765.1736	0.328	$4.66 \times 10^{-5}$
765.3883		
765.6735	0.192	$2.36 \times 10^{-5}$
765.4637		
759.8042	0.493	$8.40 \times 10^{-5}$
759.4629		
759.8969	0.322	$4.51 \times 10^{-5}$
759.4629		
760.0209	0.364	$5.35 \times 10^{-5}$
759.4629		
760.1674	0.484	$8.16 \times 10^{-5}$
759.4629		
760.3133	0.554	$1.01 \times 10^{-4}$
759.4629		

523

### 524 3.3.8 Error of differential optical depth caused jitter of $\nu$ in central optical frequency

525 The laser source of the spaceborne IPDA has a jitter of  $\nu$  central optical frequency, whereas  
 526 the online/offline emission laser spectrum has a central frequency jitter of 10MHz(Strotkamp  
 527 et al., 2019).  $\Delta\nu_{on} = \pm 10\text{MHz}$  introduces uncertainty in the Oxygen molecule absorption cross-  
 528 section  $\sigma(\nu_{on})$ , resulting in a systematic error in the optical depth. However, for solid-state  
 529 lasers, stabilizing the center wavelength within  $\pm 10\text{MHz}$  is quite easy compared to within  
 530  $\pm 1\text{MHz}$ . For example, if the center wavelength is offset by  $\pm 10\text{MHz}$ , the jitter of the emitted  
 531 laser frequency that affects the swing of the optical depth can be expressed as

532

$$[dOD(0, surface)]_{10\text{MHz}} = \int_0^{71\text{km}} \frac{0.20948p(z)}{kT(z)(1+\chi(z))} (\sigma(\nu_{on} \pm 10\text{MHz}, z) - \sigma(\nu_{off}, z)) dz$$

$$- \int_0^{71\text{km}} \frac{0.20948p(z)}{kT(z)(1+\chi(z))} (\sigma(\nu_{on}, z) - \sigma(\nu_{off}, z)) dz \quad (39)$$

533

534 It is evident from the curves of the two bands in Fig.5 that because the former is next to an  
 535 absorption line  $13069.062119\text{cm}^{-1}$  of the oxygen isotope  $^{16}\text{O}^{18}\text{O}$ , the curvature at the former  
 536 position protrudes, and the abscissa of the curve is the laser frequency (Wavelength).

537 **Table 11 Jitter in the emission laser frequency  $\nu$  causes a 10MHz change in the differential optical depth**



538

539

540

$\lambda(\text{nm})$	$dOD(v \pm 10\text{MHz}, p) - dOD(v, p)$		$\text{Max}\{ \Delta(+10\text{MHz}) ,  \Delta(-10\text{MHz}) \}$
	$ \Delta(+10\text{MHz}) $	$ \Delta(-10\text{MHz}) $	
764.6840	$6.18 \times 10^{-7}$	$9.62 \times 10^{-7}$	$9.62 \times 10^{-7}$
764.9097			
765.1600	$2.23 \times 10^{-5}$	$2.38 \times 10^{-5}$	$2.38 \times 10^{-5}$
764.9707			
765.1736	$2.00 \times 10^{-6}$	$2.81 \times 10^{-6}$	$2.81 \times 10^{-6}$
765.3883			
765.6735	$1.04 \times 10^{-6}$	$8.53 \times 10^{-7}$	$1.04 \times 10^{-6}$
765.4637			
759.8042	$4.28 \times 10^{-3}$	$2.52 \times 10^{-3}$	$4.28 \times 10^{-3}$
759.4629			
759.8969	$1.56 \times 10^{-3}$	$1.19 \times 10^{-3}$	$1.56 \times 10^{-3}$
759.4629			
760.0209	$7.71 \times 10^{-4}$	$7.76 \times 10^{-4}$	$7.76 \times 10^{-4}$
759.4629			
760.1674	$6.84 \times 10^{-4}$	$1.60 \times 10^{-3}$	$1.60 \times 10^{-4}$
759.4629			
760.3133	$3.83 \times 10^{-4}$	$9.49 \times 10^{-4}$	$9.49 \times 10^{-4}$
759.4629			

541 According to the comprehensive analysis of the above differential optical depth errors  
 542 induced in many factors, the comprehensive evaluation index items of the wavelength to be  
 543 selected are shown in Figure 12 and Figure 13.  
 544

545

**Table 12 Comprehensive of various errors at near 765nm**

Wavelength		764.6840 /764.9097	765.1600 /764.9707	765.1736 /765.3883	765.6735 /765.4637
Random error	ocean	$2.44 \times 10^{-4}$	$2.24 \times 10^{-4}$	$2.20 \times 10^{-4}$	$2.00 \times 10^{-4}$
	land	$3.55 \times 10^{-4}$	$3.30 \times 10^{-4}$	$3.24 \times 10^{-4}$	$2.96 \times 10^{-4}$
Temperature	1K	$21.54 \times 10^{-4}$	$9.31 \times 10^{-4}$	$10.16 \times 10^{-4}$	$1.43 \times 10^{-4}$
Vapor mixing ratio	20%	$5.29 \times 10^{-4}$	$4.15 \times 10^{-4}$	$4.18 \times 10^{-4}$	$2.53 \times 10^{-4}$
Energy monitor channel calibration		$1.07 \times 10^{-4}$	$0.813 \times 10^{-4}$	$0.820 \times 10^{-4}$	$0.480 \times 10^{-4}$
Echo channel calibration		$1.07 \times 10^{-4}$	$0.813 \times 10^{-4}$	$0.820 \times 10^{-4}$	$0.480 \times 10^{-4}$



Elevation 2m error	$0.458 \times 10^{-4}$	$0.372 \times 10^{-4}$	$0.374 \times 10^{-4}$	$0.236 \times 10^{-4}$
Aerosol Mie scattering	$0.903 \times 10^{-4}$	$0.756 \times 10^{-4}$	$0.857 \times 10^{-4}$	$0.837 \times 10^{-4}$
99.99% spectral purity	$0.679 \times 10^{-4}$	$0.460 \times 10^{-4}$	$0.466 \times 10^{-4}$	$0.236 \times 10^{-4}$
Frequency jitter(10MHZ)	$9.62 \times 10^{-7}$	$0.238 \times 10^{-4}$	$2.81 \times 10^{-6}$	$1.04 \times 10^{-6}$
Differential absorption cross section ( $m^2$ )	$1.80 \times 10^{-29}$	$1.46 \times 10^{-29}$	$1.47 \times 10^{-29}$	$9.25 \times 10^{-30}$
Geometrically added	$25.8 \times 10^{-4}$	$19.6 \times 10^{-4}$	$14.3 \times 10^{-4}$	$6.08 \times 10^{-4}$
Absolute error(hPa)	3.29	3.08	2.23	1.51
Relative error(%)	0.324	0.304	0.220	0.150

546

547

**Table 13 Comprehensive of various errors at near 760nm**

Wavelength		759.8042 /759.4629	759.8969 /759.4629	760.0209 /759.4629	760.1674 /759.4629	760.3133 /759.4629
Random error	ocean	$2.59 \times 10^{-4}$	$2.09 \times 10^{-4}$	$2.22 \times 10^{-4}$	$2.64 \times 10^{-4}$	$2.96 \times 10^{-4}$
	land	$3.78 \times 10^{-4}$	$3.06 \times 10^{-4}$	$3.25 \times 10^{-4}$	$3.84 \times 10^{-4}$	$4.29 \times 10^{-4}$
Temperature	1K	$26.2 \times 10^{-4}$	$4.64 \times 10^{-4}$	$9.10 \times 10^{-4}$	$27.5 \times 10^{-4}$	$47.8 \times 10^{-4}$
Vapor mixing ratio	20%	$7.68 \times 10^{-4}$	$4.86 \times 10^{-4}$	$5.38 \times 10^{-4}$	$7.03 \times 10^{-4}$	$7.95 \times 10^{-4}$
Energy monitor channel calibration		$1.91 \times 10^{-4}$	$1.25 \times 10^{-4}$	$1.40 \times 10^{-4}$	$1.96 \times 10^{-4}$	$2.28 \times 10^{-4}$
Echo channel calibration		$1.91 \times 10^{-4}$	$1.25 \times 10^{-4}$	$1.40 \times 10^{-4}$	$1.96 \times 10^{-4}$	$2.28 \times 10^{-4}$
Elevation 2m error		$0.22 \times 10^{-4}$	$0.14 \times 10^{-4}$	$0.16 \times 10^{-4}$	$0.22 \times 10^{-4}$	$0.26 \times 10^{-4}$
Aerosol Mie scattering		$1.21 \times 10^{-4}$	$1.59 \times 10^{-4}$	$2.09 \times 10^{-4}$	$2.69 \times 10^{-4}$	$3.29 \times 10^{-4}$
99.99% spectral purity		$0.840 \times 10^{-4}$	$0.451 \times 10^{-4}$	$0.535 \times 10^{-4}$	$0.816 \times 10^{-4}$	$1.01 \times 10^{-4}$
Frequency jitter(10MHZ)		$42.8 \times 10^{-4}$	$15.6 \times 10^{-4}$	$7.76 \times 10^{-4}$	$16.0 \times 10^{-4}$	$9.49 \times 10^{-4}$
Differential absorption cross section ( $m^2$ )		$2.45 \times 10^{-29}$	$1.51 \times 10^{-29}$	$1.63 \times 10^{-29}$	$2.08 \times 10^{-29}$	$2.32 \times 10^{-29}$
Geometrically added		$54.6 \times 10^{-4}$	$20.2 \times 10^{-4}$	$16.7 \times 10^{-4}$	$36.7 \times 10^{-4}$	$53.9 \times 10^{-4}$
Absolute error(hPa)		5.12	3.07	2.35	4.05	5.34
Relative error(%)		0.505	0.302	0.232	0.400	0.527

548

549 Consequently, according to Table 12 and Table 13, the pulse energy, pulse repetition, time  
 550 resolution, and distance along track are 100mJ, 100Hz, 6.25 s, and 44km, respectively. The  
 551 765.6735/765.4637 wavelength pairs are used as detection wavelength and reference  
 552 wavelength. In the 1K error temperature profile, 20% error vapor mixing ratio result in  $6.08 \times$   
 553  $10^{-4}$  error in differential optical depth, which corresponds to an absolute error in surface  
 554 pressure of 1.51hPa, therefore, it is a desirable result that the relative error of surface pressure  
 555 could be considered as 0.150%.



#### 556 4 Summary

557 The calculation process of retrieving the surface pressure from the atmospheric differential  
 558 optical depth was also discussed. The performance of the differential absorption LIDAR  
 559 model was evaluated. Owing to the influence of temperature on Oxygen absorption  
 560 coefficient and the uncertainty of atmospheric mixing ratio, maintaining the relative error of  
 561 surface atmospheric pressure below 0.1% is a challenging task. The main factors affecting the  
 562 random error of surface pressure are the low sea reflectivity, random error of low signal-to-  
 563 noise ratio, and the uneven ground, which renders the multi pulse echo unable to be  
 564 accumulated and averaged directly. Further, 765.6735/765.4637nm was selected as the  
 565 working wavelength, the pulse energy, pulse repetition, time resolution, distance along the  
 566 track resolution are 100mJ, 100Hz, 6.25 s, and 44km, respectively, while the relative error of  
 567 surface atmospheric pressure was controlled in the range of 0.2–0.3%.

568

#### 569 Author contribution

570 Guanglie Hong developed the model and Yu Dong performed the simulations, was  
 571 responsible for data processing and software code. Guanglie Hong provided part of the  
 572 manuscript and analyzed the method respectively. Huige Di supervised and modified the  
 573 manuscript.

574

#### 575 Competing interests

576 I declare that there is no conflict of interest.

#### 577 References

578

579 Brown, R. A. and Levy, G.: Ocean surface pressure fields from satellite-sensed winds, Mon.  
 580 Wea. Rev.114, doi.org/10.1175/1520-0493, 1986.

581 Korb, C. L., Schwemmer, G. K., Famiglietti, J., Walden, H. and Prasad, C.: Differential  
 582 Absorption LIDARS for Remote Sensing of Atmospheric Pressure and Temperature Profiles:  
 583 Final Report, NASA Tech. Memo. 104618, 1995.

584 Korb, C. L. and Weng, C. Y.: Differential absorption LIDAR technique for measurement of  
 585 the atmospheric pressure profile, Appl.Opt.22(23), 3759-3770, doi:10.1364/AO.22.003759,  
 586 1983.

587 Schwemmer, G. K., Dombrowski, M., Korb, C. L. Milrod, J., Walden, H. and Kagann, R. H.:  
 588 A LIDAR system for measuring atmospheric pressure and temperature profiles, Rev. Sci.  
 589 Instrum.58(12), 2226~2237, doi:10.1063/1.1139327, 1987.

590 Korb, C. L., Schwemmer, G. K., Dombrowski, M. and Weng, C. Y.: Airborne and ground  
 591 based LIDAR measurements of the atmospheric pressure profile, Appl.Opt.28(15),  
 592 3015~3020, doi:10.1364/AO.28.003015, 1989.

593 Flamant, C. N., Schwemmer, G. K., Korb, C. L., Evans, K. D. and Palm, S. P.: Pressure  
 594 Measurements using and Airborne Differential Absorption LIDAR. Part I: Analysis of the  
 595 Systematic Error Sources, J. Atmos. and Ocean. Technol.16,561~574,  
 596 doi:http://dx.doi.org/10.1175/1520-0426(1999)0162.0.CO;2, 1999.



- 597 Zaccheo, T. S., Pernini, T., Snell, H. E. and Browell, E. V.: Impact of atmospheric state  
 598 uncertainties on retrieved XCO<sub>2</sub> columns from laser differential absorption spectroscopy  
 599 measurements, *Journal of Applied remote sensing*, 083575, doi:10.1117/1.jrs.8.083575, 2014.
- 600 Crowell, S., Rayner, P., Zaccheo, S. and Moore, B.: Impacts of atmospheric state uncertainty  
 601 on O<sub>2</sub> measurement requirements for the ASCENDS mission, *Atmos. Meas. Tech.*, 8, 2685-  
 602 2697, doi:10.5194/amt-8-2685-2015, 2015.
- 603 Stephen, M. A., Krainak, M., Riris, H. and Allan, G. R.: Narrowband, tunable, frequency-  
 604 doubled, erbium-doped fiber-amplified transmitter, *Opt. Lett.*, 32, 2073-2075,  
 605 doi:10.1364/OL.32.002073, 2007.
- 606 Stephen, M. A., Mao, J. P., Abshire, J. B., Sun, X., Kawa, S. R. and Krainak, M. A.: Oxygen  
 607 Spectroscopy Laser Sounding Instrument for Remote Sensing of Atmospheric Pressure, *OSA*,  
 608 doi:10.1109/aero.2008.4526388, 2008.
- 609 Riris, H., Rodriguez, M., Allan, G. R., Hasselbrack, W. E., Stephen, M. A. and Abshire, J. B.:  
 610 Airborne LIDAR measurements of atmospheric pressure made using the oxygen A-band,  
 611 Lasers, Sources, and Related Photonic Devices Technical Digest, *OSA*,  
 612 doi:10.1117/12.892021, 2012.
- 613 Riris, H., Rodriguez, M., Allan, G. R., Hasselbrack, W. E., Mao, J. P., Stephen, M. A. and  
 614 Abshire, J.: Pulsed airborne LIDAR measurements of atmospheric optical depth using the  
 615 Oxygen A-band at 765 nm, *Appl. Opt.*, 52(25), 6369-6382, doi:10.1364/ao.52.006369, 2013.
- 616 Riris, H., Rodriguez, M., Mao, J. P., Allan, G. and Abshire, J.: Airborne demonstration of  
 617 atmospheric oxygen optical depth measurements with an integrated path differential  
 618 absorption LIDAR, *Opt. Express*, 25(23), 29307-29327, doi:10.1364/oe.25.029307, 2017.
- 619 Millán, L., Lebsock, M., Livesey, N., Tanelli, S. and Stephens, G.: Differential absorption  
 620 radar techniques: surface pressure, *Atmos. Meas. Tech.*, 7, 3959-3970, doi:10.5194/amt-7-  
 621 3959-2014, 2014.
- 622 Brown, L. R. and Plymate, C.: Experimental Line Parameters of the Oxygen A Band at 760  
 623 nm, *J. Mol. Spectrosc.*, 199, 166-179, doi:10.1006/jmsp.1999.8012, 2000.
- 624 Munk, A., Jungbluth, B., Strotkamp, M., Hoffmann, H.-D., Poprawe, R., Höffner, J. and  
 625 Lübken, F.-J.: Diode-pumped alexandrite ring laser in single-longitudinal mode operation for  
 626 atmospheric LIDAR measurements, *Opt. Express*, 26(12), 14928-14935, doi:  
 627 10.1364/oe.26.014928, 2018.
- 628 Munk, A., Strotkamp, M., Walochnik, M., Jungbluth, B., Traub, M., Hoffmann, H.-D.,  
 629 Poprawe, R., Höffner, J. and Lübken, F.-J.: Diode-pumped Q-switched Alexandrite laser in  
 630 single longitudinal mode operation with Watt-level output power, *Opt. Lett.*, 43(22), 5492-  
 631 5495, doi:10.1364/OL.43.005492, 2018.



- 632 Coney, A. T. and Damzen, M. J.: High-energy diode-pumped alexandrite amplifier  
 633 development with applications in satellite-based LIDAR, *Journal of the Optical Society of*  
 634 *America B*38(1), 209-219, doi:10.1364/JOSAB.409921, 2021.
- 635 Strotkamp, M., Munk, A., Jungbluth, B., Hoffmann, H. D. and Hoffner, J.: Diode pumped  
 636 Alexandrite laser for next generation satellite based earth observation LIDAR, *CEAS Space*  
 637 *J.*11, 413-422, doi:10.1007/s12567-019-00253-z, 2019.
- 638 Munk, A., Jungbluth, B., Strotkamp, M., Hoffmann, H.-D., Poprawe, R. and Höffner, J.:  
 639 Alexandrite laser in Q-switched, single longitudinal mode operation pumped by a fiber-  
 640 coupled diode module, *Proc. SPIE* 10896, 1089610, doi:10.1117/12.2508402, 2019.
- 641 Munk, A., Jungbluth, B., Strotkamp, M., Hoffmann, H.-D., Poprawe, R. and Höffner, J.:  
 642 Diode-pumped Alexandrite ring laser for LIDAR applications,” *Proc. SPIE* 9726, 972601,  
 643 doi:10.1117/12.2212578, 2016.
- 644 Thomas, G. M., Minassian, A., Sheng, X. and Damzen, M. J.: Diode-pumped Alexandrite  
 645 lasers in Q-switched and cavity-dumped Q-switched operation, *Opt. Express* 24(24), 27212–  
 646 27224, doi:10.1364/OE.24.027212, 2016.
- 647 Wulfmeyer, V. and ösenberg, J. B.: Single-mode operation of an injection-seeded alexandrite  
 648 ring laser for application in water-vapor and temperature differential absorption LIDAR, *Opt.*  
 649 *Lett.*21(15), 1150-1152, doi:10.1364/OL.21.001150, 1996.
- 650 Lemmerz, C., Lux, O., Reitebuch, O., Witschas, B. and Wührer, C.: Frequency and timing  
 651 stability of an airborne injection-seeded Nd:YAG laser system for direct-detection wind  
 652 LIDAR, *Appl. Opt.*56(32), 9057-9068, doi:10.1364/AO.56.009057, 2017.
- 653 Lancaster, R. S., Spinhirne, J. D. and Palm, S. P.: Laser pulse reflectance of the ocean surface  
 654 from the GLA satellite LIDAR, *Geophys. Res. Lett.*32, L22S10, doi:10.1029/2005GL023732,  
 655 2015.
- 656 Bufton, J. L., Hoge, F. E. and Swift, R. N.: Airborne measurements of laser backscatter from  
 657 the ocean surface, *Appl. Opt.*22(17), 2603- 2618, doi:10.1364/AO.22.002603, 1983.
- 658 Menzies, R. T., Tratt, D. M. and Hunt, W. H.: LIDAR In-space Technology Experiment  
 659 measurements of sea surface directional reflectance and the link to surface wind speed, *Appl.*  
 660 *Opt.*37(24), 5550-5559, doi:10.1364/AO.37.005550, 1998.
- 661 Ehret, G., Kiemle, C., Wirth, M., Amediek, A., Fix, A. and Houweling, S.: Space-borne  
 662 remote sensing of CO<sub>2</sub>, CH<sub>4</sub>, and N<sub>2</sub>O by integrated path differential absorption LIDAR: a  
 663 sensitivity analysis, *Appl. Phys. B* 90, 593–608, doi:10.1007/s00340-007-2892-3, 2008.
- 664 Standard solar constant and zero air mass solar spectral irradiance tables, ASTM international,  
 665 100 Brr Harbor Drive, United States, 2000.



- 666 Refaat, T. F., Ismail, S., Nehrir, A. R., Hair, J.W., Crawford, J. H., Leifer, I. and Shuman, T.:  
667 Performance evaluation of a 1.6- $\mu\text{m}$  methane DIAL system from ground, aircraft and UAV  
668 platforms, Opt. Express 21(25), 30415-30432, doi:10.1364/OE.21.030415, 2013.